Monthly Notices of the ROYAL ASTRONOMICAL SOCIETY

MNRAS **508,** 1888–1896 (2021) https://doi.org/10.1093/mnras/stab2739
Advance Access publication 2021 September 24

Ion acceleration to 100 keV by the ExB wave mechanism in collision-less shocks

Krzysztof Stasiewicz [1,2]★ and Bengt Eliasson[3]★

[1]*Space Research Centre, Polish Academy of Sciences, Warszawa 00-716, Poland*
[2]*Department of Physics and Astronomy, University of Zielona Góra, Zielona Gora 05-091, Poland*
[3]*SUPA, Department of Physics, University of Strathclyde, Glasgow G4 0NG, UK*

Accepted 2021 September 20. Received 2021 September 15; in original form 2021 July 8

ABSTRACT

It is shown that ions can be accelerated to about 100 keV in the direction perpendicular to the magnetic field by the ExB mechanism of electrostatic waves. The acceleration occurs in discrete steps of duration being a small fraction of the gyroperiod and can explain observations of ion energization to 10 keV at quasi-perpendicular shocks and to hundreds keV at quasi-parallel shocks. A general expression is provided for the maximum energy of ions accelerated in shocks of arbitrary configuration. The waves involved in the acceleration are related to three cross-field current-driven instabilities: the lower hybrid drift (LHD) instability induced by the density gradients in shocks and shocklets, followed by the modified two-stream (MTS) and electron cyclotron drift (ECD) instabilities, induced by the ExB drift of electrons in the strong LHD wave electric field. The ExB wave mechanism accelerates heavy ions to energies proportional to the atomic mass number, which is consistent with satellite observations upstream of the bow shock and also with observations of post-shocks in supernovae remnants. The results are compared with other acceleration mechanisms traditionally discussed in the literature.

Key words: acceleration of particles – instabilities – shock waves – turbulence – solar wind.

1 INTRODUCTION

When the solar wind plasma streaming with a speed of 400 km s^{-1} and containing protons with kinetic energy of 1 keV and the thermal spread of 20 eV interacts with the Earth's quasi-perpendicular bow shock, the ion temperature increases by a factor of 10 across the shock, while the plasma flow slows down during the compression of the solar wind plasma and magnetic field. The heating process is also associated with the appearance of energetic ions at energies 10 keV, which implies significant acceleration of a suprathermal population of the solar wind ions. The electron temperature also undergoes a rapid increase by a factor of 5 across the shock.

On the other hand, when the interplanetary magnetic field is in the quasi-parallel direction to the shock normal, an extended upstream foreshock region (Greenstadt, Le & Strangeway 1995; Eastwood et al. 2005) is formed, containing ULF waves, turbulence, non-linear structures, and field-aligned beams. In addition to the electron and ion heating comparable to that occurring in quasi-perpendicular shocks, observations upstream of the quasi-parallel shocks show energetic ions accelerated to hundreds keV, indicating a three to four orders of magnitude increase of the kinetic energy.

The energetic ions observed in quasi-parallel shocks are traditionally believed to be energized in a diffusive shock acceleration process. The key assumptions of this model are: (i) the solar wind ions are preheated at the shock and partially reflected upstream, (ii) there are moving barriers in the upstream region that reflect these ions back to the bow shock. After multiple bouncing between these barriers the ions gain energy through the Fermi acceleration mechanism (Fermi 1949; Bell 1978; Lee & Fisk 1982; Burgess, Möbius & Scholer 2012; Otsuka et al. 2018). Because the interplanetary shocks that could provide the upstream reflecting boundary are rare phenomena there has been a continuous search for other obstacles, such as for example foreshock transients, needed for the Fermi process to work at the bow shock. In a new attempt, Turner et al. (2018) have suggested that hot flow anomalies (Thomsen et al. 1988; Liu et al. 2016) observed occasionally in the solar wind could make such upstream barriers, or traps where the energization occurs autogenously.

All mechanisms relying on the Fermi process require non-local magnetic traps/mirrors, which are difficult to justify for energetic ions observed on every satellite passage upstream of the quasi-parallel shock, viz., whenever the interplanetary magnetic field changes direction to quasi-parallel. Any acceleration relying on multiple bouncing would require interaction times much longer than those implied by the observations. Thus, a local process that does not require moving magnetic mirrors, or electrostatic field barriers, would be more suitable to explain ion acceleration at quasi-parallel shocks.

It has been recently shown (Stasiewicz 2020; Stasiewicz & Eliasson 2020a,b; Stasiewicz et al. 2021) that charged particle heating and acceleration in collision-less shocks of arbitrary orientation are related to the wave electric fields of drift instabilities triggered by shock compression of the plasma. It is a local process that can be summarized as follows:

Shock compressions of the density N and the magnetic field B → diamagnetic current → lower hybrid drift (LHD) instability → electron E×B drift → modified two-stream (MTS) and electron

★ E-mail: krzy.stasiewicz@gmail.com (KS); bengt.eliasson@strath.ac.uk (BE)

cyclotron drift (ECD) instabilities → heating: quasi-adiabatic ($\chi_j < 1$), stochastic ($\chi_j > 1$), acceleration ($\chi_j \gg 1$).

The stochastic heating and acceleration of particle species with charge q_j and mass m_j ($j = e$ for electrons, p for protons, i for general ions) is controlled by the function

$$\chi_j(t, \mathbf{r}) = \frac{m_j}{q_j B^2} \mathrm{div}(\mathbf{E}_\perp) \tag{1}$$

that depends on the m_j/q_j ratio and is also a measure of the charge non-neutrality. It is a generalization of the heating condition from earlier works of Karney (1979), McChesney, Stern & Bellan (1987), Balikhin, Gedalin & Petrukovich (1993), Vranjes & Poedts (2010), where the divergence is reduced to the directional gradient $\partial E_x/\partial x$. The charged particles are magnetized (adiabatic) for $|\chi_j| < 1$, demagnetized (subject to non-adiabatic heating) for $|\chi_j| \gtrsim 1$, and selectively accelerated to high perpendicular velocities when $|\chi_j| \gg 1$.

The term 'stochastic' is here used in the sense of chaos theory applied to a statistical ensemble of particles. At a certain threshold value of $|\chi_j|$, particle orbits become unstable and neighbouring phase space trajectories deviate from each other exponentially in time with positive Lyapunov exponents. This makes the system sensitive to initial conditions and even though it is deterministic for a single particle, it appears to be stochastic for a statistical ensemble of particles. The chaotic motion typically sets in for $|\chi_j| \gtrsim 1$ when the interacting waves have frequencies comparable to or below the cyclotron frequency, $f \lesssim f_{cj}$, such as electrostatic shocks and non-linear structures (Balikhin et al. 1993; Stasiewicz, Lundin & Marklund 2000) and low-frequency periodic electrostatic waves (McChesney et al. 1987). At higher wave frequencies $f \gg f_{cj}$ (Karney 1979), chaotic motion sets in for particles having velocities near the phase velocity, $v \gtrsim v_{ph} = \omega/k$ with a threshold value $E/B \gtrsim (f_{cj}/f)^{1/3} v_{ph}/4$ for chaotic motion, which can be written in dimension-less variables as $|\chi_j| \gtrsim \Omega^{2/3}/4$ with $\Omega = f/f_{cj}$ and $|\chi_j| = m_j kE/q_j B^2$. Wave frequencies near cyclotron harmonics (Fukuyama et al. 1977) can also lead to resonant acceleration of particles with $v \gtrsim v_{ph}$ to form high-velocity tails in the distribution function. Thus, at high frequencies we have the formation of an 'acceleration lane' indicated by a green line in Fig. 1.

Previous simulations have shown that ions at perpendicular bow shocks are stochastically bulk heated with typical values of $\chi_p \sim 60$ produced by the electric fields of the LHD instability. Electrons can also be heated stochastically on electron cyclotron drift waves. However, in most cases they undergo a quasi-adiabatic heating process, $T_{e\parallel} \approx T_{e\perp} \propto B^\alpha$, where $\alpha = 1/3 - 2/3$ (Stasiewicz & Eliasson 2020a,b).

The aim of this paper is to show that ions can be accelerated to hundreds keV by electrostatic waves in the frequency range from the proton gyrofrequency f_{cp} to the electron gyrofrequency f_{ce} associated with the three cross-field, current-driven LHD, MTS, and ECD instabilities mentioned above. The acceleration mechanism requires $\chi \gg 1$ and can increase velocity of some ions by the E×B drift velocity due to the wave electric field, i.e. by the speed $\widetilde{V}_E = \widetilde{E}_\perp/B$ (Sugihara & Midzuno 1979; Dawson et al. 1983; Ohsawa 1985). The E×B wave mechanism is related to the surfing mechanism at shocks (Katsouleas & Dawson 1983; Zank et al. 1996; Ucer & Shapiro 2001; Shapiro & Ucer 2003), which requires wide front of coherent waves and acceleration is done through multiple ion reflections between the shock and the upstream region (Zank et al. 1996; Shapiro, Lee & Quest 2001). In contradistinction, the stochastic E×B mechanism is associated with the stochastic condition (1) and works on much shorter time-scales at a fraction of a cyclotron period and much shorter spatial scales. This makes it possible for protons to be accelerated to 10 eV → 100 keV on intermittent and bursty waves observed at shocks.

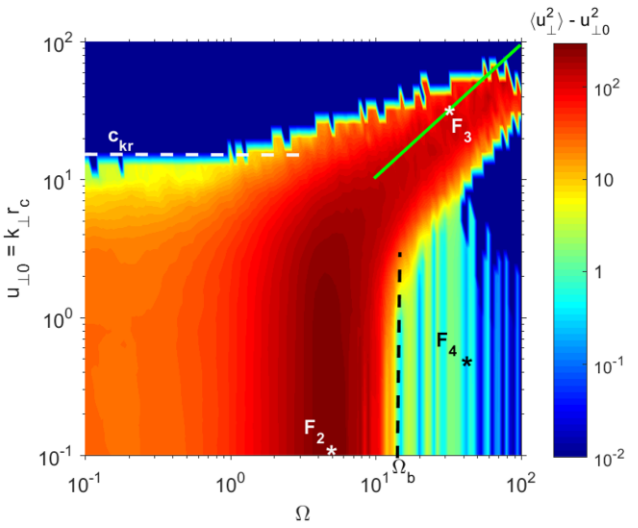

Figure 1. A colourmap of stochastic energization of ions showing the difference $\langle u_\perp^2 \rangle - u_{\perp 0}^2$ between the normalized squared speed at the end of the test particle simulation and the initial value $u_{\perp 0}^2 = k_x^2 r_c^2$ after 1 cyclotron period for initially Maxwell distributed ions in an electrostatic wave with normalized electric field amplitude $\widetilde{\chi} = 30$. Bulk heating takes place for $\Omega < \Omega_b \approx 13$ (vertical dashed line) and $u_{\perp 0} < c_{kr} \approx 15$ (horizontal dashed line), while for $u_{\perp 0} \gtrsim c_{kr}$, there is significant heating only for thermal velocity comparable to the wave phase velocity, or $u_{\perp 0} \sim \Omega$ in the normalized variables (diagonal green line) leading to a distribution function having a high energy tail of ions. Positions marked with asterisks refer to Figs 2–4 where the acceleration process is studied in detail.

2 STOCHASTIC ION HEATING AND ACCELERATION

Stochastic heating and acceleration of ions by electrostatic waves can be studied with the test-particle simulation setup developed by Stasiewicz & Eliasson (2020a,b). We use test particles to represent ions which are accelerated by the prescribed electrostatic wave and magnetic field, but which do not contribute to the fields or interact with other ions. The position $\mathbf{r}$ and velocity $\mathbf{v}$ of an ion with mass m and charge q are determined by the Lorentz equation $m\mathrm{d}\mathbf{v}/\mathrm{d}t = q(\mathbf{E} + \mathbf{v} \times \mathbf{B}_0)$ together with $\mathrm{d}\mathbf{r}/\mathrm{d}t = \mathbf{v}$. Associated with the magnetic field $\mathbf{B}_0 = (0, 0, B_0)$ in the spacecraft frame there is a macroscopic electric field E_{y0} that convects the plasma ions (and electrons) into an electrostatic wave $\widetilde{E}_x = E_{x0} \sin(\omega_D t - k_x x)$ with wavenumber $k_x = 2\pi/\lambda$ with λ being the wavelength, and the Doppler shifted frequency ω_D. By a Galilei transformation to the plasma reference frame in which the convection electric field is zero (Stasiewicz & Eliasson 2020a), and using dimension-less variables with time normalized by ω_c^{-1}, space by k_x^{-1}, and velocity by ω_c/k_x with $\omega_c = qB_0/m$ being the angular ion cyclotron frequency, the normalized equations of motion on component form for a test ion are

$$\frac{\mathrm{d}u_x}{\mathrm{d}t} = \widetilde{\chi} \sin(\Omega t - x) + u_y, \tag{2}$$

$$\frac{\mathrm{d}u_y}{\mathrm{d}t} = -u_x, \tag{3}$$

$$\frac{\mathrm{d}x}{\mathrm{d}t} = u_x, \qquad \frac{\mathrm{d}y}{\mathrm{d}t} = u_y. \tag{4}$$

The system has two dimension-less parameters: the normalized wave frequency in the plasma frame $\Omega = (\omega_D - k_x E_{y0}/B_0)/\omega_c$, and the normalized wave amplitude

$$\widetilde{\chi} = \frac{E_{x0}}{B_0}\frac{k_x}{\omega_c}, \tag{5}$$

which is consistent with the stochastic heating function (1) for a single wave mode. The initial gyration velocity of the ion is $(v_x, v_y) = (v_{x0}, v_{y0})$, and in normalized variables $(u_x, u_y) = (u_{x0}, u_{y0})$.

For a statistical description of the ions, we follow the procedure outlined in previous works (Stasiewicz & Eliasson 2020a,b), and carry out a set of test particle simulations for $M = 1\,000$ ions, which initially are Maxwell distributed in velocity and uniformly random distributed in space. The initial conditions are described by a 2D Maxwellian distribution function of velocity components perpendicular to the magnetic field, which in the normalized variables can be written as

$$F = \frac{1}{2\pi u_{\perp 0}^2}\exp\left(-\frac{(u_x^2+u_y^2)}{2u_{\perp 0}^2}\right). \tag{6}$$

Here, the initial normalized ion thermal speed is

$$u_{\perp 0} = v_{T0}k_\perp/\omega_c = k_\perp r_c \tag{7}$$

with the thermal speed $v_{T0} = (2T_0/m)^{1/2}$, the initial Larmor radius $r_c = v_{T0}/\omega_c$, the initial ion temperature T_0, and wavenumber $k_\perp = k_x$. The value of $u_{\perp 0}$ is used as an input parameter to the test-particle simulations, in addition to Ω and $\widetilde{\chi}$.

For each ion in the initial Maxwell distribution, the system (2)–(4) is advanced in time using a Störmer–Verlet scheme (Press et al. 2007). Simulations are carried out for several values of the normalized wave frequency Ω in the range 10^{-1} to 10^2, and for $u_{\perp 0}$ spanning 10^{-1} to 10^2. The normalized amplitude of the electrostatic wave is set to $\widetilde{\chi} = 30$, which is typical for lower hybrid waves measured at the Earth's bow shock (Stasiewicz & Eliasson 2020a). The simulations are run for a relatively short time of one cyclotron period, motivated by the observations of rapid ion heating at the bow shock. The normalized mean squared speeds $\langle u_\perp^2\rangle = k_\perp^2\langle v_\perp^2\rangle/\omega_c^2$ at the end of the simulations are calculated as

$$\langle u_\perp^2\rangle = \frac{1}{M}\sum_{l=1}^{M}\left(u_{x,l}^2 + u_{y,l}^2\right). \tag{8}$$

Fig. 1 shows a colour plot of the difference $\langle u_\perp^2\rangle - u_{\perp 0}^2$ between the normalized squared speed $\langle u_\perp^2\rangle$ at the end of the simulation and the initial value $u_{\perp 0}^2 = k_\perp^2 r_c^2$.

It can be seen in Fig. 1 that the bulk heating region is most intense for frequencies $\Omega < \Omega_b \approx 13$ and wavenumbers obeying $k_\perp r_c < c_{kr} \approx 15$. For protons the frequency limit corresponds to frequencies less than one-third of the lower hybrid frequency ($\Omega_{lh} \approx 43$), and the wavenumber limit corresponds to wavelengths $\lambda_\perp = 2\pi/k_\perp$ satisfying

$$r_c \lesssim 2\lambda_\perp. \tag{9}$$

Thus, the stochastic heating of the bulk plasma becomes inefficient when the thermal ion gyroradius becomes larger than two wavelengths. Both limits Ω_b and c_{kr} would shift to larger values for maps computed with larger $\widetilde{\chi}$ (Stasiewicz & Eliasson 2020a).

There is also a region of the acceleration of suprathermal ions from the tail of the distribution function that occurs along the green line $k_\perp r_c \approx \Omega$, for $\Omega \gtrsim 10$ as seen in Fig. 1. Ions along this line, hereafter referred to as the acceleration lane, have gyration speed $v_{\perp 0}$ that matches the phase speed of waves (Fukuyama et al. 1977; Karney 1979)

$$v_{\perp 0} \approx r_c\omega_c = \omega/k_\perp = f\lambda_\perp, \tag{10}$$

which links $v_\perp$ with electrostatic waves (f, $\lambda_\perp$) that can accelerate these ions. While the bulk heating is done stochastically for all ions satisfying (9), the perpendicular acceleration to high velocities along the acceleration lane (10) is selective and requires some speed and phase matching.

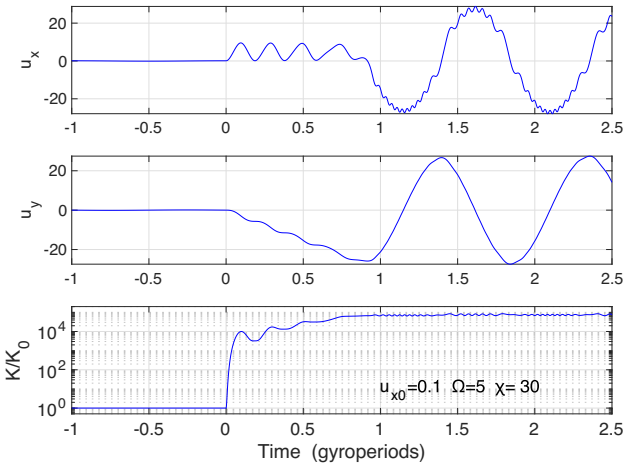

Figure 2. Acceleration of an ion in the bulk heating region (marked as 'F_2' in the colourmap in Fig. 1) with initial velocity $u_{x0} = k_x r_c = 0.1, u_{y0} = 0$ by wave $\Omega = 5$ and $\widetilde{\chi} = 30$. The wave is switched on at $t = 0$. Panels show velocity components u_x, u_y, and the kinetic energy ratio K/K_0. Energy increase by a factor of 10^4 is achieved within half of the wave period, or 1/10 of the gyroperiod.

2.1 The physics of the ExB wave acceleration

In order to understand the physics of the stochastic energization we have analyzed individual ion trajectories for cases marked 'F_2', 'F_3', and 'F_4' in Fig. 1. Fig. 2 shows a solution of equations (2)–(4) for one ion with speed $u_{x0} = 0.1$ and $u_{y0} = 0$ injected into a wave at frequency $\Omega = 5$ and amplitude $\widetilde{\chi} = 30$ in the bulk heating region marked as 'F_2' in Fig. 1. The ion energy is increased by factor 10^4 within a half oscillation period of the electrostatic wave, corresponding to 1/10 gyroperiod. In the beginning, the ion makes cyclotron motion with small velocity $u_\perp = 0.1$ (not visible in the plot) until $t = 0$, when the wave is switched on. The velocity $u_x(t)$ shows polarization drift response $\propto \mathrm{d}E_x/\mathrm{d}t$, in the wave electric field, before resuming the cyclotron motion after one gyroperiod. The velocity u_y increases with time as the E×B velocity $v_y(t) = -\widetilde{E}_x(t, x)/B_0$ to the maximum value in the normalized variables $u_y \approx (E_{x0}/B_0)(k_x/\omega_c) \equiv \widetilde{\chi}$.

The mechanism described above will be called 'χ-acceleration', or the 'E×B acceleration', because the maximum acceleration capacity corresponds to the value of $\widetilde{\chi}$, in normalized units, or to the E×B velocity computed with the wave electric field, i.e. $\widetilde{V}_E = \widetilde{E}_\perp/B$ in physical units. This limiting value for the acceleration was previously found by Sugihara & Midzuno (1979) and Dawson et al. (1983), who analysed the same equations (2)–(4) in the wave frame. This mechanism has been also used in simulations of ion heating by large amplitude magnetosonic waves by Lembége et al. (1983). The energization capacity is then

$$K_E \lesssim \frac{m}{2}\left[v_{\perp 0}^2 + (\widetilde{E}_\perp/B)^2\right], \tag{11}$$

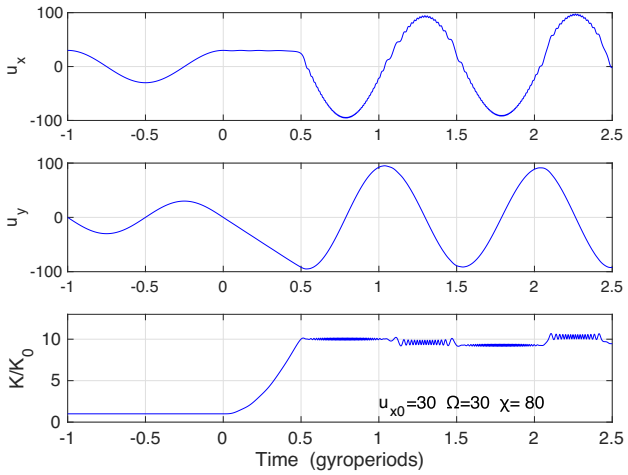

Figure 3. The ion exiting Fig. 2 with $u_{x0} = 30$ encounters a new wave $\Omega = 30$, $\widetilde{\chi} = 80$, and is energized by a factor of 10 within a half gyroperiod. The position in the colourmap in Fig. 1 is marked as 'F_3'.

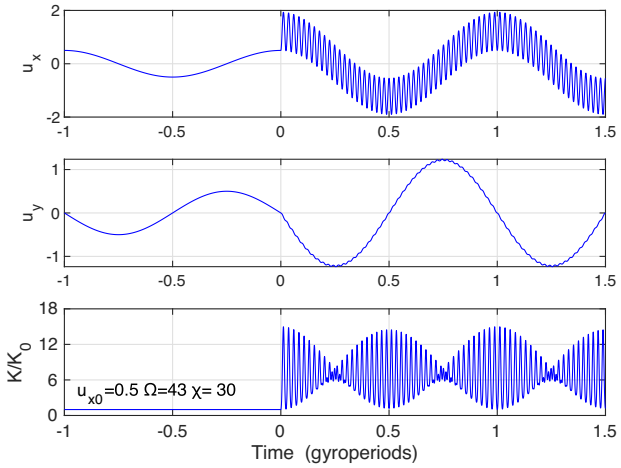

Figure 4. Acceleration of a low energy ion with $u_{x0} = 0.5$ by a lower hybrid wave $\Omega = 43$, $\widetilde{\chi} = 30$. A proton is accelerated by a factor of 6 within 1/40 of a gyroperiod. The position in the colourmap in Fig. 1 is marked as 'F_4'.

which is mass dependent. This equation is a general limit for the perpendicular acceleration of ions in quasi-parallel and quasi-perpendicular shocks as will be shown in Section 3. It is applicable both to the bulk heating region, where $v_{\perp 0} = v_T$ is the ion thermal speed, and also to the acceleration lane, where $v_{\perp 0}$ of suprathermal ions corresponds to the wave phase speed, or equivalently to $u_{\perp 0} = k_\perp r_c \sim \Omega$.

The acceleration capacity offered by equation (11) can be determined from the electric field measured on the *Magnetospheric Multiscale* (*MMS*) spacecraft (Burch et al. 2016) by Ergun et al. (2016), Lindqvist et al. (2016). For the quasi-parallel shock analysed in this paper, this limit amounts to $K_E \sim 200$ keV shown in Fig. 6(e) below, which corresponds well to the measured proton fluxes shown in Fig. 6(a).

The amplitudes of the wave electric field $\widetilde{E}$ and of $\widetilde{\chi}$ increase with frequency, which makes higher frequency waves more suitable for acceleration of ions to higher energies. The lower frequency waves $\Omega < 1$ ($f < f_c = \omega_c/2\pi$) are less efficient accelerators because of smaller amplitudes. They also require interaction times of a few cyclotron periods, but long coherent wave trains are unlikely to occur in turbulent shock plasma.

2.2 The acceleration lane and the polarization drift

The ion accelerated to $u_x = 30$ in the first step can encounter a new wave on the acceleration lane with frequency $\Omega = 30$ and get additional energization as shown in Fig. 3. The second wave with $\widetilde{\chi} = 80$ would energize the ion by a factor of 10 within a half gyroperiod. In this case $u_x(t)$ is constant, and $u_y(t)$ increases steady to the value of $\widetilde{\chi}$, i.e. to the E×B speed in the wave field, until the cyclotron motion is resumed after $t = 0.5$. The second wave could be in any direction. The only requirement is that the phase speed of wave matches the perpendicular speed of an ion on an arbitrary phase of the gyration. The acceleration could continue along the acceleration lane, but it requires larger Ω and larger $\widetilde{\chi}$ values on each subsequent step. The acceleration works equally well for an ensemble of waves with different frequencies and random phases (Stasiewicz et al. 2021).

By checking the effectiveness of the χ-acceleration for different input parameters, it is found that around the acceleration lane ($u_{\perp 0} \sim \Omega$) the approximate energization rate is

$$K/K_0 \sim 1 + (\widetilde{\chi}/u_{\perp 0})^2, \tag{12}$$

which could continue to arbitrary high velocities $u_\perp$, providing there exist waves with sufficiently high amplitudes $\widetilde{\chi} \sim u_\perp$. The above expression is in fact equivalent to equation (11) derived in a different way.

Yet another type of acceleration occurs for low energy ions in waves $\Omega > \Omega_b$, around the lower hybrid frequency $\Omega \approx 43$ (position 'F_4' in Fig. 1). It is seen in Fig. 4 that a proton with velocity $u_{x0} = 0.5$ is rapidly accelerated by an average factor of 6 within the wave period (1/40 of the cyclotron period), but it executes quivering motion related to the polarization drift seen in panel u_x. This means that the frequency Ω_b in Fig. 1 represents in fact the boundary between the strong E×B drift response for $\Omega < \Omega_b$, and a weaker polarization drift response for $\Omega > \Omega_b$.

Equation (10) implies that ions with perpendicular energy K_0 and mass m are on the acceleration lane when

$$K_0 = \frac{m}{2} f^2 \lambda_\perp^2. \tag{13}$$

A handy formula for ions with atomic mass $A = m_i/m_p$ is

$$K_{0[\mathrm{keV}]} \approx 10 A f_{[\mathrm{kHz}]}^2 \lambda_{\perp[\mathrm{km}]}^2, \tag{14}$$

which applies also for electrons with $A = 1/1836$. Using this expression we can find, for example, that protons with energy 1 keV could be accelerated by waves $f = 10$ Hz, $\lambda_\perp \approx 33$ km, which are in the lower hybrid range. On the other hand, protons at energy 1000 keV would interact with waves $f = 1$ kHz and $\lambda_\perp \approx 10$ km, which could be found in the ECD frequency range. Oxygen ions ($A = 16$) at energy of 16 MeV would interact with the same waves ($f \approx 1$ kHz and $\lambda_\perp \approx 10$ km) as 1 MeV protons.

The wave phase velocity $f\lambda_\perp = \omega/k_\perp$ in (13) determines the energy of ions prone to the acceleration by waves. The LHD waves have maximum frequency $\omega_{lh} = (\omega_{ce}\omega_{ci})^{1/2}$ and wavenumbers $k_\perp(r_e r_i)^{1/2} \sim 1$, as shown by Daughton (2003) and Umeda & Nakamura (2018), so the phase speed of LHD waves is $v_{ph} = f\lambda_\perp \sim (v_{Te}v_{Ti})^{1/2}$. Here, $v_{Te} = (2T_e/m_e)^{1/2}$ is the electron thermal speed, $v_{Ti} = (2T_i/m_i)^{1/2}$ is the ion thermal speed and the gyroradii are: $r_e = v_{Te}/\omega_{ce}$, $r_i = v_{Ti}/\omega_{ci}$. This gives the maximum energy of ions accelerated by LHD waves

with $\Omega \approx \omega_{lh}/\omega_{cp} \lesssim 43$ as

$$K^{\rm LHD} \lesssim 1.5 \left(\frac{m_i}{m_e} T_e T_i\right)^{1/2}, \quad (15)$$

where the factor 1.5 is an empirical factor that fits the energy of the accelerated ions in perpendicular shocks as shown in Section 3. This value can be compared with factor of 2 implied by equation (12) when $\widetilde{\chi} \sim u_{\perp 0} < 43$. For temperatures $T_e \approx 40$ eV, $T_i \approx 400$ eV we obtain the proton energy $K \sim 8$ keV, which is typically observed as the upper acceleration energy at quasi-perpendicular shocks.

2.3 Comparison with other models

The processes described in Sections 2.1 and 2.2 have some components in common with the surfing mechanism introduced by Katsouleas & Dawson (1983) for the relativistic acceleration of electrons in laser plasmas. The surfing idea is based on work by Sagdeev (1966) and has been elaborated further in many papers (Zank et al. 1996; Shapiro et al. 2001; Ucer & Shapiro 2001; Shapiro & Ucer 2003; Eliasson, Dieckmann & Shukla 2005). It has been also used to explain acceleration in shocks of supernova remnants (McClements et al. 2001) and acceleration of cosmic rays (Kichigin 2013). Namely, a charged particle can be trapped and transported in the potential well during extended time, which leads to the acceleration in the perpendicular direction until the resulting Lorentz force exceeds the electrostatic force of the wave, and the particle becomes un-trapped.

The surfing acceleration (Shapiro et al. 2001; Shapiro & Ucer 2003) takes place at quasi-perpendicular shocks, where the electrostatic waves propagate in the sunward (x-) direction, while the ions are carried by the shock and accelerated parallel to the shock front (in the y-direction). The acceleration is mainly by the DC convection electric field E_{y0}, and partly by the wave electric field E_x for trapped ions. The surfing mechanism requires wide front of coherent waves, with several ion gyroradii width in the y-direction, and acceleration is done through multiple ion reflections between the shock and the upstream region (Shapiro et al. 2001). The surfing mechanism of Katsouleas & Dawson (1983) offered 'unlimited acceleration' to relativistic energies. Because of practical difficulty for wide enough fronts of coherent waves to be formed both in the laboratory plasma and at the turbulent bow shock, the ideas of efficient surfing acceleration have not been confirmed in the laboratory or space. Another problem with surfing acceleration is that the wave electric field strengths are likely above the threshold for the modulational instability that leads to the breakup of the wave and eventually wave collapse. This would make turbulent field structures that destroy the phase trapping necessary for the surfing acceleration mechanism.

In contrast to the surfing acceleration models, the E×B is coupled with the stochastic condition (1), and for large χ values, energization by a factor 10^4 can be achieved within the wave period f^{-1} as seen in Fig. 2. It corresponds to 1/40 of the proton gyroperiod for lower hybrid waves in Fig. 4.

The E×B wave mechanism does not require wide wave fronts as the classical surfing acceleration (Katsouleas & Dawson 1983; Ucer & Shapiro 2001; Shapiro & Ucer 2003), and the acceleration can be done by bursty intermittent wave packets as observed in satellite data shown in Fig. 6. It has been demonstrated recently (Stasiewicz et al. 2021) that an ensemble of waves with a wide range of frequencies and random phases can accelerate protons from 10 eV to 100 keV within a few gyroperiods. The proton energy flux obtained from simulations accurately reproduces the measured ion spectra at the bow shock.

The E×B wave mechanism supported by equation (1) operates not only at quasi-perpendicular and quasi-parallel shocks (Stasiewicz & Eliasson 2020a,b), but also, for example, in laboratory plasma during ion heating by drift waves (McChesney et al. 1987), and in the ion heating regions of the topside ionosphere (Stasiewicz et al. 2000).

Both shock surfing acceleration and shock drift acceleration (Ball & Melrose 2001) rely on macroscopic convection electric field to accelerate ions. The present mechanism uses only the wave electric field. The wave amplitudes measured in shocks above the lower hybrid frequency are typically 10–30 times larger than the convection field, which ensures rapid acceleration and high energization ratios. As will be shown later, it is most efficient in parallel shocks, where the average convection field is zero.

Other models require some pre-acceleration or heating, before they can be operational. The heating map in Fig. 1 can explain both, a rapid heating of 10 eV ions and further acceleration of high energy ions along the acceleration lane. As mentioned earlier, the E×B acceleration works within a fraction of the gyroperiod, while the shock surfing acceleration (Zank et al. 1996; Ucer & Shapiro 2001; Shapiro & Ucer 2003) requires many cyclotron periods, and the diffusive shock acceleration (Bell 1978; Lee & Fisk 1982) requires even much longer times.

In the next section, we show measurements of waves and turbulence at quasi-perpendicular and quasi-parallel shocks, which indicate that these waves are likely to χ-heat bulk of ions and also accelerate some ions to high energies by the E×B mechanism presented above.

3 COMPARISON WITH OBSERVATIONS

Fig. 5 shows 1 min of burst-mode data from the quasi-perpendicular bow shock. This is one of nine multiple shock encounters analysed by Stasiewicz & Eliasson (2020a). The particle data from the Fast Plasma Investigation (FPI) (Pollock et al. 2016) shown in panel (a) are taken at position (10.2, 13.4, −1.8) R_E GSE (geocentric solar ecliptic). The Alfvén Mach number was 7.2, the electron plasma beta $\beta_e \approx 1.1$, and the ion beta $\beta_i \approx 2.5$, on the upstream (right) side of the shock. The angle between the magnetic field and the geocentric radial direction (a proxy to the shock normal) was 124°. Overplotted are the ion and electron temperatures, and the acceleration capacity of LHD waves given by (15). This equation provides accurate values for the maximum energy of protons accelerated at quasi-perpendicular shocks observed by MMS.

Active heating and acceleration of ions, seen in the elevated ion temperature in panel (a) coincides with strong LHD waves at 14:31:57−14:32:12 UTC. In this region, ions are accelerated up to about 4 keV. The heating region coincides with the region of the smallest values of the gradient scale lengths $L_B = B|\nabla B|^{-1}$ for the magnetic field and $L_N = N|\nabla N|^{-1}$ for the electron density N, both normalized by the thermal ion gyroradius r_p and shown in panel (d). The condition $L_N/r_p < (m_p/m_e)^{1/4} < 1$ corresponds to strong LHD instability (Davidson et al. 1977; Drake, Huba & Gladd 1983; Gary 1993). The gradient scales are derived directly from four point measurements using the method of Harvey (1998). It is seen that the values for L_N derived for the cold solar wind, after 14:32:10 UTC are not reliable, and the values for L_B should be used instead. Panel (c) shows the amplitude of the measured electric field in the range 0–4000 Hz with peak values above 100 mV m^{-1}.

Almost the whole time interval in Fig. 5 the plasma is unstable for the LHD instability, as seen in the wave spectrogram in panel (b) with the most intense waves in the frequency range $f_{cp} - f_{lh}$. These waves are indeed responsible for the ion energization

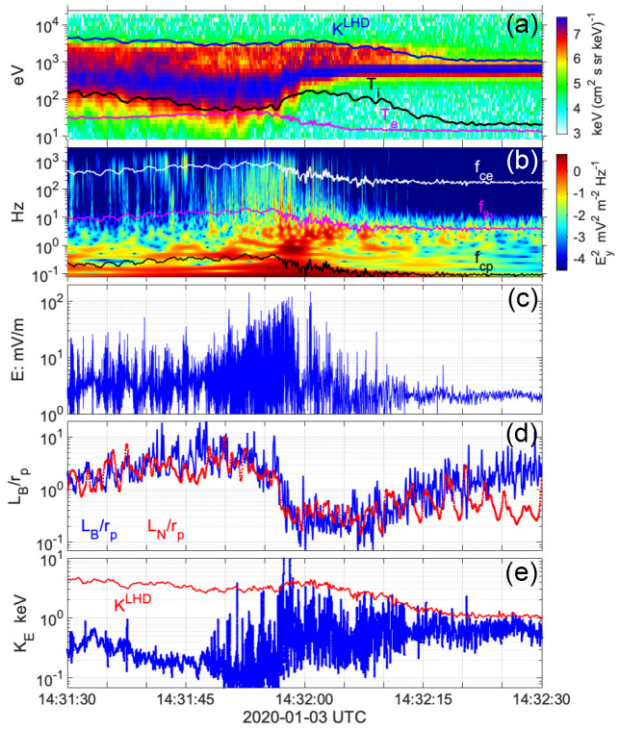

Figure 5. Quasi-perpendicular shock observations by the MMS3 spacecraft. (a) Time versus energy spectrogram of the ion differential energy flux measured by FPI. Overplotted are the electron and ion temperatures and the acceleration capacity of LHD waves given by equation (15). (b) Time versus frequency spectrogram of the E_y (GSE) component of the electric field. Overplotted are the electron cyclotron f_{ce}, the lower hybrid f_{lh}, and the proton cyclotron f_{cp}. (c) Amplitude of the measured electric field in the frequency range 0-4000 Hz. (d) The measured gradient scale of the magnetic field L_B and of the plasma density L_N normalized with the thermal proton gyroradius r_p. (e) The energization capacity of waves given by (11) for waves $f < 20$ Hz in the lower hybrid frequency range. Overplotted is the acceleration capacity given by equation (15).

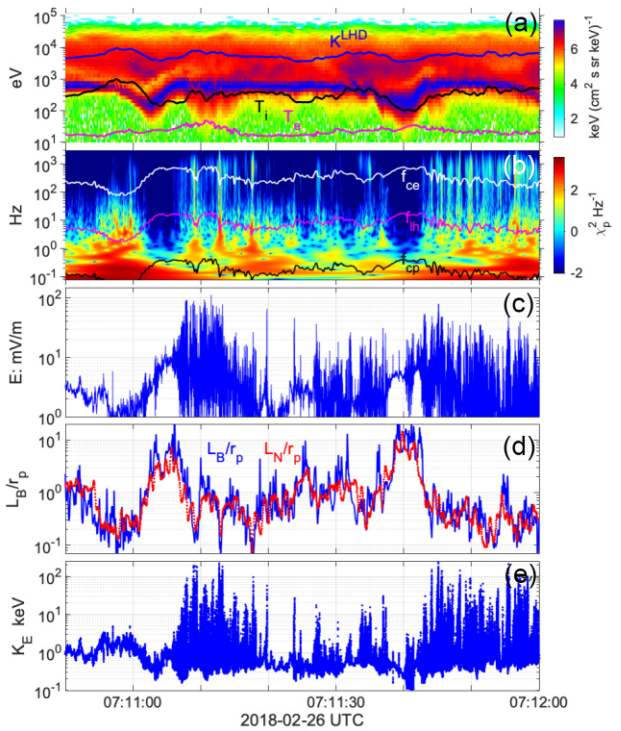

Figure 6. Quasi-parallel shock observations by the *MMS3* spacecraft. (a) Ion energy flux spectrogram measured by FPI in the energy range 10 eV–20 keV combined with EIS measurements in the energy range 20–100 keV. Overplotted are electron and ion temperatures and the acceleration capacity of LHD waves given by equation (15). (b) Time versus frequency spectrogram of χ_p. Overplotted are the plasma frequencies: f_{ce}, f_{lh}, and f_{cp}. (c) Amplitude of the measured electric field in the frequency range 0–4000 Hz. (d) Gradient scales L_B and L_N derived from measurements and normalized with r_p. (e) The energization capacity of waves given by (11) for waves in the measured frequency range 0–4000 Hz.

through the E×B mechanism presented in Section 2. This can be seen in panel (e). The acceleration capacity of waves below 20 Hz derived with (11) corresponds exactly to the limiting energy of ions in panel (a), and coincides also with the other independent estimate (15). The frequencies plotted in panel (b) are proportional to B so the magnetic structure of the shock can be inferred from the frequency plots. Complementary discussion and overview of data for this case can be found elsewhere (Stasiewicz & Eliasson 2020b).

Fig. 6 shows 1 min of data from a long duration quasi-parallel shock measured by the *MMS3* spacecraft. The satellite was at position (12.6, −3.9, 4.1) R_E, where the Alfvén Mach number was in the range 1–6 with the average of 3, the average electron plasma beta $\beta_e \sim 0.7$, and the ion beta $\beta_i \sim 5$. The data represents a couple of shocklets, i.e. compressions of the plasma density and of the magnetic field associated with retardation of the solar wind beam as seen in panel (a).

The time versus frequency spectrogram of χ_p given by equation (1) and shown in Fig. 6(b) is derived from measurements of the electric field sampled at the rate 8192 s^{-1}. The computed values reach $\chi_p \approx$ 1800 for higher frequency ECD waves. Details of the technique for computing div(**E**) from four point measurements are discussed by Stasiewicz & Eliasson (2020a,b).

Fig. 6(d) shows L_B/r_p and L_N/r_p similar to Fig. 5(c). Here, there is good agreement between the magnetic field and density length scales. The LHD waves in panel (b) are in excellent correlation with regions $L_N/r_p \lesssim (m_p/m_e)^{1/4} \sim 6$, where the LHD instability should theoretically occur.

The energization limit for the measured waves computed with (11) is shown in panel (e). We see excellent agreement between the theoretical maximum energy ∼100 keV in panel (e) and the measured energy spectra in panel (a). The average gyroradius of a 40 keV proton in this time interval is 2000 km. Because of large gyroradii of energetic ions, which tap energy from intermittent waves over large spatial areas, direct spatial correlations between ∼ 100 keV ions in panel (a) and accelerating waves in panel (c) are not expected.

A major difference between this case and the previous one is that here ions are accelerated to up to about 100 keV, while in the quasi-perpendicular shock the ions were only accelerated to about 4 keV. The amplitudes of the electric field $E \sim 100$ mV m^{-1} are similar in both types of shocks as seen in Figs 5(c) and 6(c). The large difference in the maximum acceleration between quasi-perpendicular and quasi-parallel shocks seems to be due to the different interaction times the ions have with the waves. At perpendicular shocks, the solar wind rapidly convects across the shock, and the relatively short interaction time is comparable to one ion gyroperiod. Here, the acceleration is done mainly by LHD waves having frequencies $f < 20$ Hz, up to the limit (15), or to the limit (11).

In parallel shocks, energetic ions meander or bounce between the shocklets in the upstream region and repetitively interact with higher frequency waves at increasing frequencies during much longer times. This would stepwise increase their energy to the limit (11) through the same χ-acceleration mechanism, along the acceleration lane of Fig. 1.

In order to increase proton energy by 100 keV in bursty waves electric fields of 100 mV m^{-1} an effective interaction length of minimum 1000 km is required. As mentioned above, a 40 keV proton for the case in Fig. 6 has a gyroradius of 2000 km with circumference of the orbit 12 000 km. This implies that intermittent bursty waves that fill the path of the proton orbit by the linear filling factor of 0.1 could increase the proton energy from 40 to 140 keV during one gyroperiod. Waves at amplitude of 50 mV m^{-1} that fill on average only 0.05 of the proton orbit would require interaction time of 4 gyroperiods, and so on. In view of the spatiotemporal density of large amplitude waves seen in Fig. 6(c), the above estimates are reasonable and provide strong support for the proposed acceleration mechanism.

Waves of similar amplitudes as shown in Figs 5(c) and 6(c), i.e. $|\mathbf{E}| \sim 100$ mV m^{-1}, at higher frequencies are measured on every bow shock crossing whenever local acceleration/heating of ions is observed. This can be readily verified by using the Quicklook plots in burst mode for the *MMS* mission; see relevant links in Data availability statement.

As mentioned in Section 1, the wave generation process in both cases is initiated by the density gradients associated with the quasi-perpendicular shock in Fig. 5 and with quasi-parallel shocklets in Fig. 6, which produce diamagnetic currents that cause first the LHD instability (Davidson et al. 1977; Gary 1993; Daughton 2003) which has a lower threshold than the MTS and ECD instabilities.

The wave spectrograms in Figs 5(b) and 6(b) can be divided into four frequency bands: the magnetosonic waves below f_{cp}, the lower hybrid drift (LHD) waves in the frequency range $f_{cp} - f_{lh}$, the modified two-stream (MTS) instability in the range $f_{lh} - f_{ce}$, and the electron cyclotron drift (ECD) waves around and above f_{ce}. Other wave modes like whistlers and ion acoustic waves may also contribute in the spectrograms. The displayed spectrograms are in the spacecraft frame, so there may be some mixing and overlap of modes due to the frequency Doppler shift of short wavelengths by the bulk plasma flow ~250 km s^{-1}.

In the frequency range $f_{cp} - f_{lh}$ there are magnetic field fluctuations, which are also observed in simulations (Daughton 2003), in the magnetotail (Ergun et al. 2019), and at the magnetopause (Graham et al. 2019). This could mean that LHD waves coexist with ion whistler waves created in the density striations by mode conversion (Rosenberg & Gekelman 2001; Eliasson & Papadopoulos 2008; Camporeale, Delzanno & Colestock 2012) from LHD waves, or with magnetosonic fluctuations. Such whistler waves, propagating upstream are seen in Fig. 5. Lower hybrid waves and whistlers can be also produced by ring distributions (Winske & Daughton 2015) of ions reflected from the bow shock, but Fig. 5(d) and analysis of similar waves in Fig. 6 indicate that the driving mechanism for LHD waves at both shocks are density gradients rather than the reflected ion beams. However, the magnetosonic waves in the frequency range $f_{cp} - f_{lh}$ are equally efficient ion accelerators as demonstrated by Lembége et al. (1983), Lembége & Dawson (1984), and Ohsawa (1985).

The enhanced electric field of the LHD or magnetosonic waves produces strong E×B drifts of electrons only, because the ions are not subject to this drift due to their large gyroradius in comparison to the width of drift channels. When the electron-ion drift exceeds

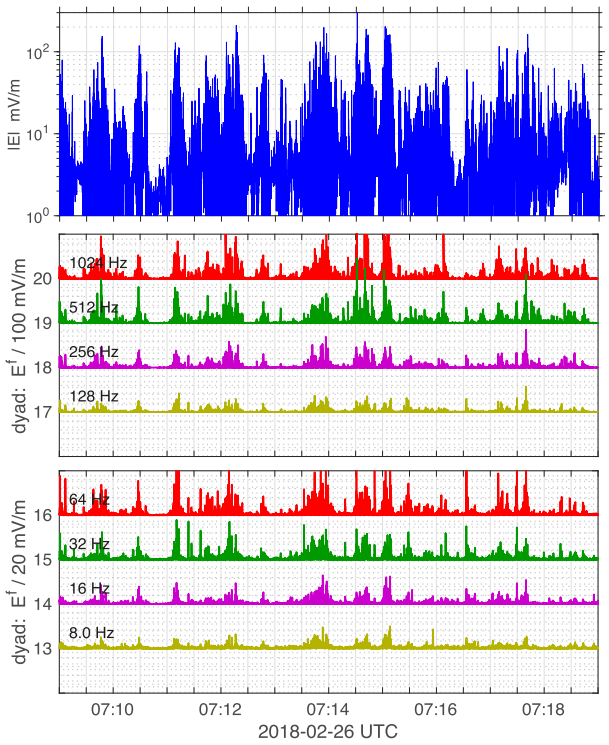

Figure 7. The electric field vector measured in a quasi-parallel bow shock with amplitude shown in the upper panel is decomposed into discrete dyads E^f in the frequency range $f = 8 - 1024$ Hz. The lower hybrid frequency, f_{lh} is in the range 8–16 Hz. Fig. 6 covers 07:11-07:12 UTC interval of this 10 min event.

the ion thermal speed and becomes a significant fraction of the electron thermal speed, the MTS (Wu et al. 1983; Umeda et al. 2014; Muschietti & Lembége 2017) and ECD instabilities (Lashmore-Davies & Martin 1973; Muschietti & Lembége 2013; Janhunen et al. 2018) are triggered at frequencies from above f_{lh} to a few harmonics of f_{ce}. Such waves with electric field amplitudes of ~ 100 mV m^{-1} at higher frequencies are commonly observed at the bow shock by different spacecraft (Wilson III et al. 2010; Breneman et al. 2013; Mozer & Sundqvist 2013; Goodrich et al. 2018).

Note the vertical striations in panels 5(b) and 6(b) that start from ~0.5 Hz (LHD instability) and extend up through the MTS and ECD instabilities to 3 kHz, indicating co-location and common origin of these instabilities. The MTS waves propagate obliquely to the magnetic field and produce parallel electric field component that may be responsible for the isotropization of the electron distribution (Stasiewicz & Eliasson 2020b).

The spatial structures and the frequency content of the wave electric field can also be studied with orthogonal wavelet decomposition (Mallat 1999) shown in Fig. 7. The upper panel shows the amplitude of the electric field vector measured by *MMS3* at sampling rate 8192 s^{-1} during 600 s of the burst mode that includes a 70 s interval of Fig. 6. The electric field vector is decomposed into discrete frequency layers (dyads) with orthogonal wavelets that form $f = 2^{-s} f_N$ hierarchy ($s = 0, 1, 2, \ldots$) starting from the Nyquist frequency (f_N is half of the sampling frequency). The decomposition forms complete in the sense that the sum of all components gives the original signal, and the orthogonality means that the time integral of products of any pairs of dyads having different frequencies is zero. The amplitude of

the decomposed signal is shown for eight frequencies in the range 8–1024 Hz.

The lower hybrid frequency is in the range $f_{lh} \sim$ 8–16 Hz, but the LHD waves may be Doppler upshifted and observed also at 32–64 Hz. It is seen that they have amplitudes of 10–20 mV m^{-1}. The higher frequency waves, 64–256 Hz, that we associate with the MTS instability discussed above have amplitudes 50–80 mV m^{-1}, while waves in the vicinity of the electron cyclotron frequency $\sim$512 Hz have peak amplitudes of 100 mV m^{-1}. Waves in channel 1024 Hz, and in channels 2048–4096 Hz (not shown here), which correspond to higher harmonics of f_{ce} and to the proton plasma frequency, f_{pp}, may contain Debye length structures $\sim$15 m with amplitudes up to 200 mV m^{-1}. Such wavelengths are expected for higher harmonics ECD waves and for ion acoustic waves above f_{pp} (Muschietti & Lembége 2013).

The sequential triggering and co-location of the LHD–MTS–ECD instabilities seen very well in Fig. 7 can be also explained by considering the expression for the E×B drift velocity for ions with gyroradius r_c in a spatially varying electric field $E_x \propto \sin(k_\perp x)$ (Chen 2016)

$$\mathbf{V}_E = \frac{\mathbf{E}\times\mathbf{B}}{B^2}\left(1-\frac{1}{4}k_\perp^2 r_c^2\right). \quad (16)$$

Ions with large gyroradius would have greatly reduced E×B drift velocity in comparison with small gyroradius electrons. When the ratio $\lambda_\perp/r_p \lesssim \pi$, the ion electric drift vanishes, and the sole electron drift would produce strong cross-field current that could drive the above-mentioned instabilities. Actually, the conditions for the onset of the diamagnetic LHD instability on density gradients, and the complete quenching of the E×B ion drift on short wavelengths are similar

$$\frac{L_N}{r_p} \sim \frac{\lambda_\perp}{r_p} \lesssim 6, \quad (17)$$

which means that the chain of the instabilities LHD–MTS–ECD could be enforced by steepening of magnetosonic shock waves to smaller wavelengths, even in the absence of sufficient diamagnetic currents.

One should be also aware, that the E×B drift of ions (16) is a different phenomenon than the E×B wave energization mechanism (11) discussed in this paper. The E×B wave heating of ions starts, when the E×B drift stops.

The ions accelerated by the χ-mechanism in quasi-parallel shocks can diffuse through the magnetopause and form the quasi-trapped population of energetic ions inside. This idea is opposite to claims that the energetic ions observed upstream of the bow shock represent leakage of ions from the magnetosphere (Mauk et al. 2019). The dependence $\widetilde{\chi} \propto m/q$, and mass dependence of the energization (11,13) could explain observations that heavy ions in the C,N,O group have fluxes larger than protons at high energies (Stasiewicz et al. 2013; Turner et al. 2018). This is also consistent with observation of heavy ion temperatures $T_i \propto m_i/m_p$ in post-shocks of supernova remnants (Raymond et al. 2017; Miceli et al. 2019; Gedalin 2020). However, there are also other explanations for the preferential heating of heavy ions (Zank et al. 1996, 2001; Shapiro et al. 2001).

4 CONCLUSIONS

This research is based on the well-established concepts of the stochastic heating laid down in a seminal paper by Karney (1979), represented by equation (1), and on the E×B wave acceleration limit by large amplitude waves found by Sugihara & Midzuno (1979) and Dawson et al. (1983), represented by equation (11). By combining these two concepts with multipoint *MMS* measurements (Burch et al. 2016), we have shown that solar wind ions are bulk heated by the stochastic mechanism (1) both in quasi-perpendicular and in quasi-parallel shocks confirming the previous results of Stasiewicz & Eliasson (2020a,b). The perpendicular χ-heating is a rapid process and may be accomplished within a fraction of a gyroperiod. Selected suprathermal ions with perpendicular gyration velocity equal to the phase speed of electrostatic waves $v_\perp \approx \omega/k_\perp$ can be accelerated to velocities of the E×B drift in the wave field, $\widetilde{V}_E = \widetilde{E}_\perp/B$. The acceleration requires waves with the stochastic heating parameter $\widetilde{\chi} = (\widetilde{E}_\perp/B)(k_\perp/\omega_c) \gg 1$ and occurs in discrete steps on intermittent waves observed in shocks. The process could bring some ions to energies of $\sim$100 keV as shown in this paper and in Stasiewicz et al. (2021).

In collision-less shocks, waves that accelerate ions are produced by the three cross-field current-driven LHD, MTS, and ECD instabilities, in the frequency range $f_{cp} - f_{ce}$, which are seen in Fig. 6(b). The instabilities are cascade-triggered by diamagnetic currents induced by the density gradients created both in perpendicular shocks and in shocklets that form parallel shocks.

The short interaction time with waves at perpendicular shocks limits the maximum energy of protons to $\sim$10 keV and the acceleration is done by LHD waves only, while the multistep acceleration by higher frequency waves $f_{lh} - f_{ce}$ in parallel shocks can bring some ions to energies of hundreds keV, as observed in *MMS* data at the Earth's bow shock. The general expression (11) provides an explanation of the observed maximum energy of ions accelerated in shocks of arbitrary configuration.

It is suggested that ions accelerated in quasi-parallel shocks to hundreds keV diffuse into the magnetosphere and form the quasi-trapped energetic ion population.

The χ or E×B mechanism accelerates heavy ions to energies proportional to the atomic mass number, which is consistent with satellite observations upstream of the bow shock and also with observations of ion temperatures in post-shocks of supernova remnants.

ACKNOWLEDGEMENTS

BE acknowledges support from the Engineering and Physical Sciences Research Council (EPSRC, UK), grant EP/M009386/1.

DATA AVAILABILITY

The data supporting the results in this article are available through the MMS Science Data Center at the Laboratory for Atmospheric and Space Physics (LASP), University of Colorado, Boulder: https://lasp.colorado.edu/mms/sdc/public/. The data were processed with the IRFU-Matlab analysis package available at https://github.com/irfu/irfu-matlab.

REFERENCES

Balikhin M., Gedalin M., Petrukovich A., 1993, Phys. Rev. Lett., 70, 1259
Ball L., Melrose D. B., 2001, Publ. Astron. Soc. Austr., 18, 361
Bell A. R., 1978, MNRAS, 182, 147
Breneman A. W., Cattell C. A., Kersten K., Paradise A., Schreiner S., Kellogg P. J., Goetz K., Wilson III L. B., 2013, J. Geophys. Res., 118, 7654
Burch J. L., Moore R. E., Torbert R. B., Giles B. L., 2016, Space Sci. Rev., 199, 1
Burgess D., Möbius E., Scholer M., 2012, Space Sci. Rev., 173, 5
Camporeale E., Delzanno G. L., Colestock P., 2012, J. Geophys. Res., 117, A10315

Chen F. F., 2016, Introduction to Plasma Physics and Controlled Fusion. Springer, Berlin
Daughton W., 2003, Phys. Plasmas, 10, 3103
Davidson R. C., Gladd N. T., Wu C., Huba J. D., 1977, Phys. Fluids, 20, 301
Dawson J. M. et al., 1983, Phys. Rev. Lett., 50, 1455
Drake J. F., Huba J. D., Gladd N. T., 1983, Phys. Fluids, 26, 2247
Eastwood J. P., Lucek E. A., Mazelle C., Meziane K., Narita Y., Pickett J., Treumann R. A., 2005, Space Sci. Rev., 118, 41
Eliasson B., Papadopoulos K., 2008, J. Geophys. Res., 113, A09315
Eliasson B., Dieckmann M. E., Shukla P. K., 2005, New J. Phys., 7, 136
Ergun R. E. et al., 2016, Space Sci. Rev., 199, 167
Ergun R. E. et al., 2019, J. Geophys. Res., 124, 10085
Fermi E., 1949, Phys. Rev., 75, 1169
Fukuyama A., Momota H., Itatani R., Takizuka T., 1977, Phys. Rev. Lett., 38, 701
Gary S. P., 1993, Theory of Space Plasma Microinstabilities. Cambridge Univ. Press, Cambridge
Gedalin M., 2020, ApJ, 900, 171
Goodrich K. A. et al., 2018, J. Geophys. Res., 123, 9430
Graham D. B. et al., 2019, J. Geophys. Res., 124, 8727
Greenstadt E. W., Le G., Strangeway R. J., 1995, Adv. Space Phys., 15, 71
Harvey C. C., 1998, in Paschmann G., Daly P. W., eds, ISSI Reports, Analysis Methods for Multi-spacecraft Data. Vol. SR-001, ESA, Paris, p. 307
Janhunen S., Smolyakov A., Sydorenko D., Jimenez M., Kaganovich I., Raitses Y., 2018, Phys. Plasmas, 25, 082308
Karney C. F. F., 1979, Phys. Fluids, 22, 2188
Katsouleas T., Dawson J. M., 1983, Phys. Rev. Lett., 51, 392
Kichigin G., 2013, Adv. Space Res., 51, 309
Lashmore-Davies C., Martin T., 1973, Nucl. Fusion, 13, 193
Lee M. A., Fisk L. A., 1982, Space Sci. Rev., 32, 205
Lembége B., Dawson J. M., 1984, Phys. Rev. Lett., 53, 1053
Lembége B., Ratliff S. T., Dawson J. M., Ohsawa Y., 1983, Phys. Rev. Lett., 51, 264
Lindqvist P. A. et al., 2016, Space Sci. Rev., 199, 137
Liu T. Z., Turner D. L., Angelopoulos V., Omidi N., 2016, J. Geophys. Res., 121, 5489
Mallat S., 1999, A Wavelet Tour of Signal Processing. Academic Press, Cambridge
Mauk B. H. et al., 2019, J. Geophys. Res., 124, 5539
McChesney J. M., Stern R., Bellan P. M., 1987, Phys. Rev. Lett., 59, 1436
McClements K. G., Dieckmann M. E., Ynnerman A., Chapman S. C., Dendy R. O., 2001, Phys. Rev. Lett., 87, 255002
Miceli M. et al., 2019, Nat. Astron., 3, 236
Mozer F. S., Sundqvist D., 2013, J. Geophys. Res., 118, 5415
Muschietti L., Lembége B., 2013, J. Geophys. Res., 118, 2267
Muschietti L., Lembége B., 2017, Ann. Geophys., 35, 1093
Ohsawa Y., 1985, Phys. Fluids, 28, 2130
Otsuka F., Matsukiyo S., Kis A., Nakanishi K., Hada T., 2018, ApJ, 853, 117
Pollock C. et al., 2016, Space Sci. Rev., 199, 331
Press W. H., Teukolsky S. A., Vetterling W. T., Flannery B. P., 2007, Numerical Recipes: The Art of Scientific Computing. Cambridge Univ. Press, New York
Raymond J. C., Winkler P. F., Blair W. P., Laming J. M., 2017, ApJ, 851, 12
Rosenberg S., Gekelman W., 2001, J. Geophys. Res., 106, 28,867
Sagdeev R. Z., 1966, Rev. Plasma Phys., 4, 23
Shapiro V. D., Ucer D., 2003, Planet. Space Sci., 51, 665
Shapiro V. D., Lee M. A., Quest K. B., 2001, J. Geophys. Res., 106, 25023
Stasiewicz K., 2020, MNRAS, 496, L133
Stasiewicz K., Eliasson B., 2020a, ApJ, 903, 57
Stasiewicz K., Eliasson B., 2020b, ApJ, 904, 173
Stasiewicz K., Lundin R., Marklund G., 2000, Phys. Scripta, T84, 60
Stasiewicz K., Markidis S., Eliasson B., Strumik M., Yamauchi M., 2013, Europhys. Lett., 102, 49001
Stasiewicz K., Eliasson B., Cohen I. J., Turner D. L., Ergun R. E., 2021, J. Geophys. Res., 126, e2021JA029477
Sugihara R., Midzuno Y., 1979, J. Phys. Soc. Japan, 47, 1290
Thomsen M. F., Gosling J. T., Bame S. J., Quest K. B., Russell C. T., Fuselier S. A., 1988, J. Geophys. Res., 93, 11311
Turner D. L. et al., 2018, Nature, 561, 206
Ucer D., Shapiro V. D., 2001, Phys. Rev. Lett., 87, 075001
Umeda T., Nakamura T. K. M., 2018, Phys. Plasmas, 25, 102109
Umeda T., Kidani Y., Matsukiyo S., Yamazaki R., 2014, Phys. Plasmas, 21, 022102
Vranjes J., Poedts S., 2010, MNRAS, 408, 1835
Wilson III L. B., Cattell C. A., Kellogg P. J., Goetz K., Kersten K., Kasper J. C., Szabo A., Wilber M., 2010, J. Geophys. Res., 115, A12104
Winske D., Daughton W., 2015, Phys. Plasmas, 22, 022102
Wu C. S., Zhou Y. M., Tsai S.-T., Guo S. C., Winske D., Papadopoulos K., 1983, Phys. Fluids, 26, 1259
Zank G. P., Pauls H. L., Cairns I. H., Webb G. M., 1996, J. Geophys. Res., 101, 457
Zank G. P., Rice W. K. M., le Roux J. A., Matthaeus W. H., 2001, ApJ, 556, 494

This paper has been typeset from a TEX/LATEX file prepared by the author.